Supplementary Materials

Observation of Robust Interlayer Biexcitons in Twisted Homobilayer Superlattices

Haihong Zheng[1], Xing Xie[1], Shaofei Li[1], Shula Chen[2], Jun He[1], Zongwen Liu[3], Chang-Tian Wang[4], Jian-Tao Wang[4], Xidong Duan[5], Yuerui Lu[6,*], Anlian Pan[2,*] & Yanping Liu[1,7,8*]

1. *School of Physics and Electronics, Hunan Key Laboratory for Super-microstructure and Ultrafast Process, Central South University, 932 South Lushan Road, Changsha, Hunan 410083, People's Republic of China*
2. *College of Materials Science and Engineering, Hunan University, Changsha, Hunan 410082, P. R. China*
3. *School of Chemical and Biomolecular Engineering, The University of Sydney, NSW 2006, Australia*
4. *Beijing National Laboratory for Condensed Matter Physics, Institute of Physics, Chinese Academy of Sciences, Beijing 100190, People's Republic of China*
5. *Hunan Institute of Optoelectronic Integration, College of Materials Science and Engineering, Hunan University, Changsha, Hunan 410082, People's Republic of China*
6. *Research School of Engineering, College of Engineering and Computer Science, The Australian National University, Canberra, Australian Capital Territory, 2601 Australia*
7. *State Key Laboratory of High-Performance Complex Manufacturing, Central South University, 932 South Lushan Road, Changsha, Hunan 410083, People's Republic of China*
8. *Shenzhen Research Institute of Central South University, Shenzhen 51800, People's Republic of China*

* Correspondence and requests for materials should be addressed to email: yuerui.lu@anu.edu.au; anlian.pan@hnu.edu.cn; liuyanping@csu.edu.cn

Supplementary Note 1. Fabrication of twisted WSe_2 homobilayers on Au arrays

The WSe_2/WSe_2 homobilayers were created using a wet-transfer technique involving a polymethyl methacrylate (PMMA) film. The process involved transferring one layer of WSe_2 onto another, aligning the crystal axes of the top monolayer with those of the bottom monolayer under an optical microscope. The resulting two-dimensional material was then attached to an Au nanorod by controlling the rate of water evaporation at the interface. The rotation angle between the two monolayers was determined using second harmonic generation (SHG) with a 1064 nm pulsed laser as the excitation light source. To further optimize the samples, they were annealed at 300 ℃ for 3 hours under high vacuum conditions.

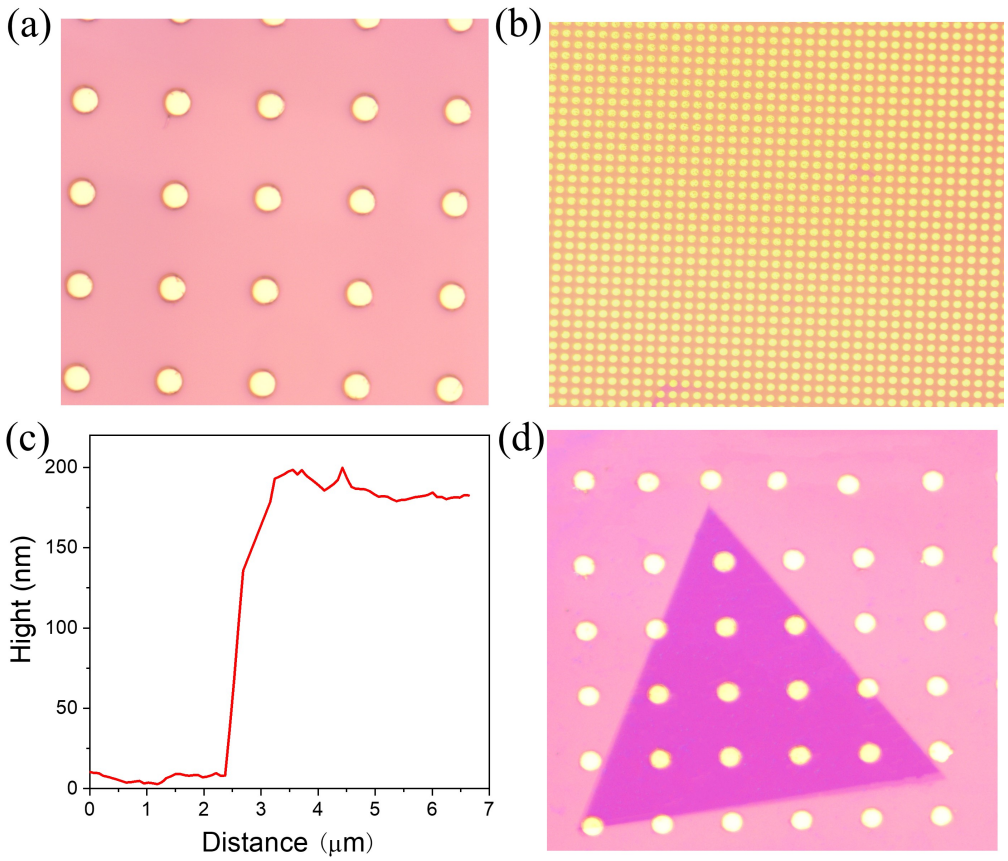

Supplementary Fig. 1 (a) Preparation of Au nanorod arrays (NRAs) by thermal evaporation. (b) Preparation of Au nanorod arrays with different spacings. (c) AFM characterization of Au nanorod. (d) The optical microscopy image of Au NRAs covered by as-transferred WSe_2/WSe_2 homobilayers.

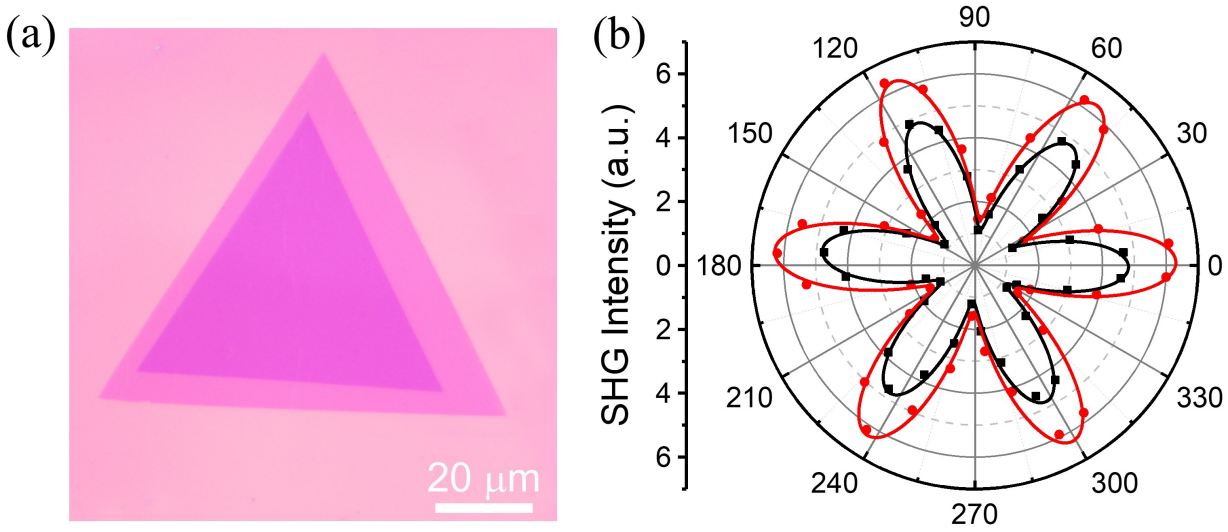

Supplementary Fig. 2 (a) Optical microscopy image of the WSe_2/WSe_2 homobilayer with a twist angle of 1.5°. (b) Measured and fitted the SHG signals of the WSe_2 monolayer area on the top and bottom of the sample to determine that the twist angle between the WSe_2 bilayers is close to zero.

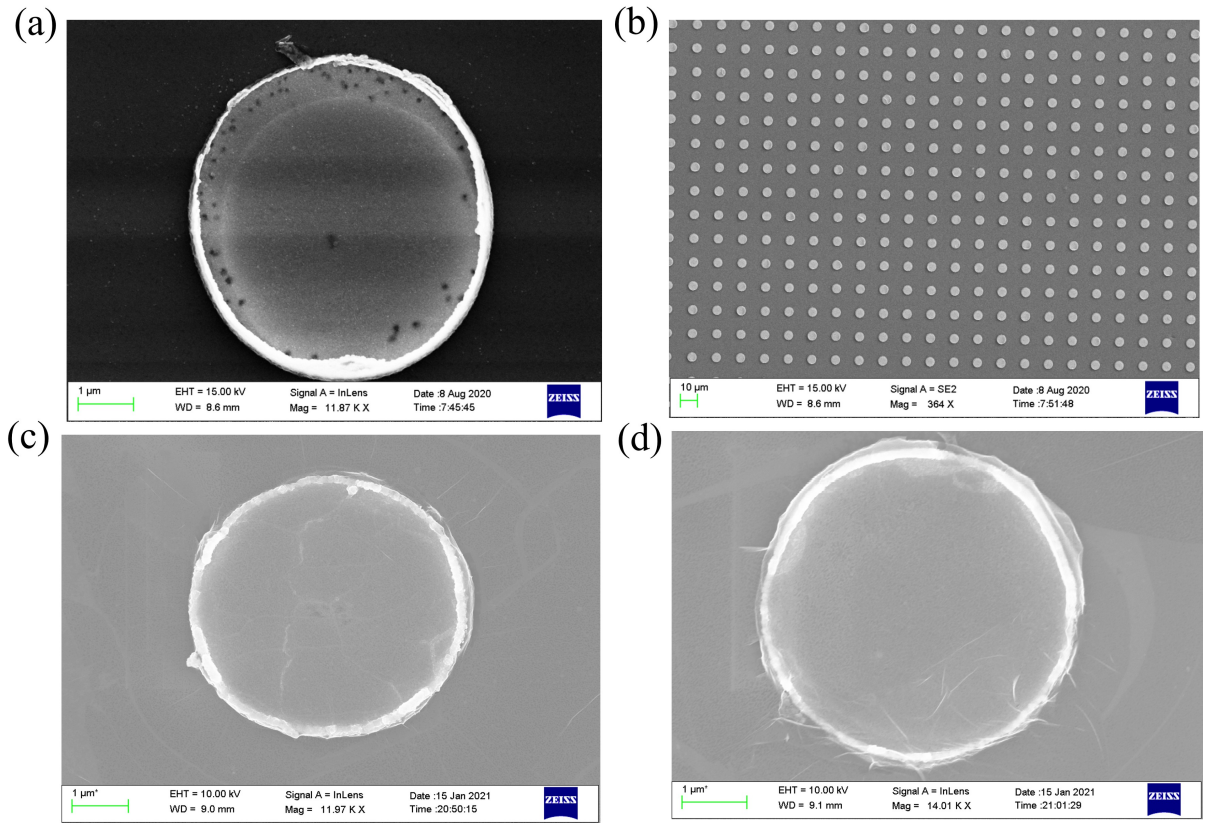

Supplementary Fig. 3 (a, b) SEM images of Au nanorod arrays (NRAs). (c, d) SEM images of the twisted WSe_2/WSe_2 homobilayer on the Au NRAs.

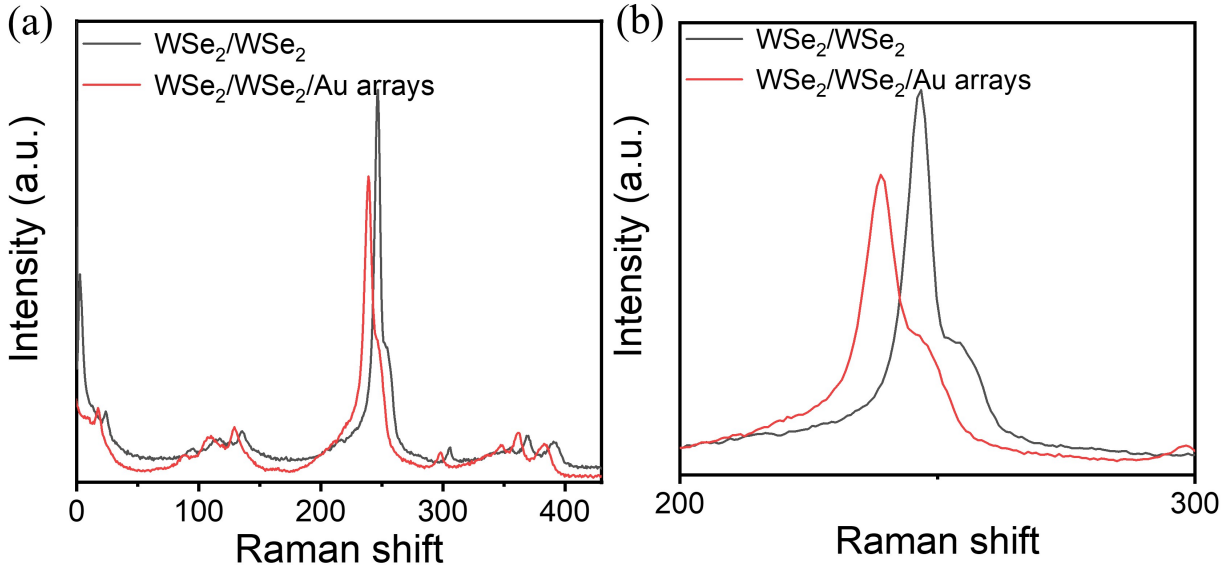

Supplementary Fig. 4 (a, b) The Raman spectra of the WSe_2/WSe_2 homobilayers in strained and unstrained regions at room temperature.

Supplementary Note 2. Moiré superlattice modulates the optical properties.

The moiré potential depth is an indicator of the potential energy contained within a moiré pattern. A moiré pattern is generated when two material layers are stacked and twisted in relation to each other. The twist angle denotes the angle between the two layers, and the number of layers stacked on top of each other determines the number of layers. To calculate the period of the moiré superlattice a_m, the following equations can be used:

$$a_m = \frac{a_{WSe_2}}{\sqrt{2-2\cos(\theta)}} \quad (1)$$

where a is the lattice constant of the WSe_2 monolayer (0.328 nm). The torsion angle between layers is represented by θ. Thus, for the sample with a twist angle of $1.5 \pm 0.5°$, the moiré period is 12 ± 0.2 nm. As per the formula, the depth of the moiré potential can be adjusted by the moiré period (a_m). Hence, with a smaller moiré period, the moiré potential becomes deeper. This implies that for samples with

larger twist angles within the small angle range, the moiré period decreases, resulting in a deeper moiré potential.

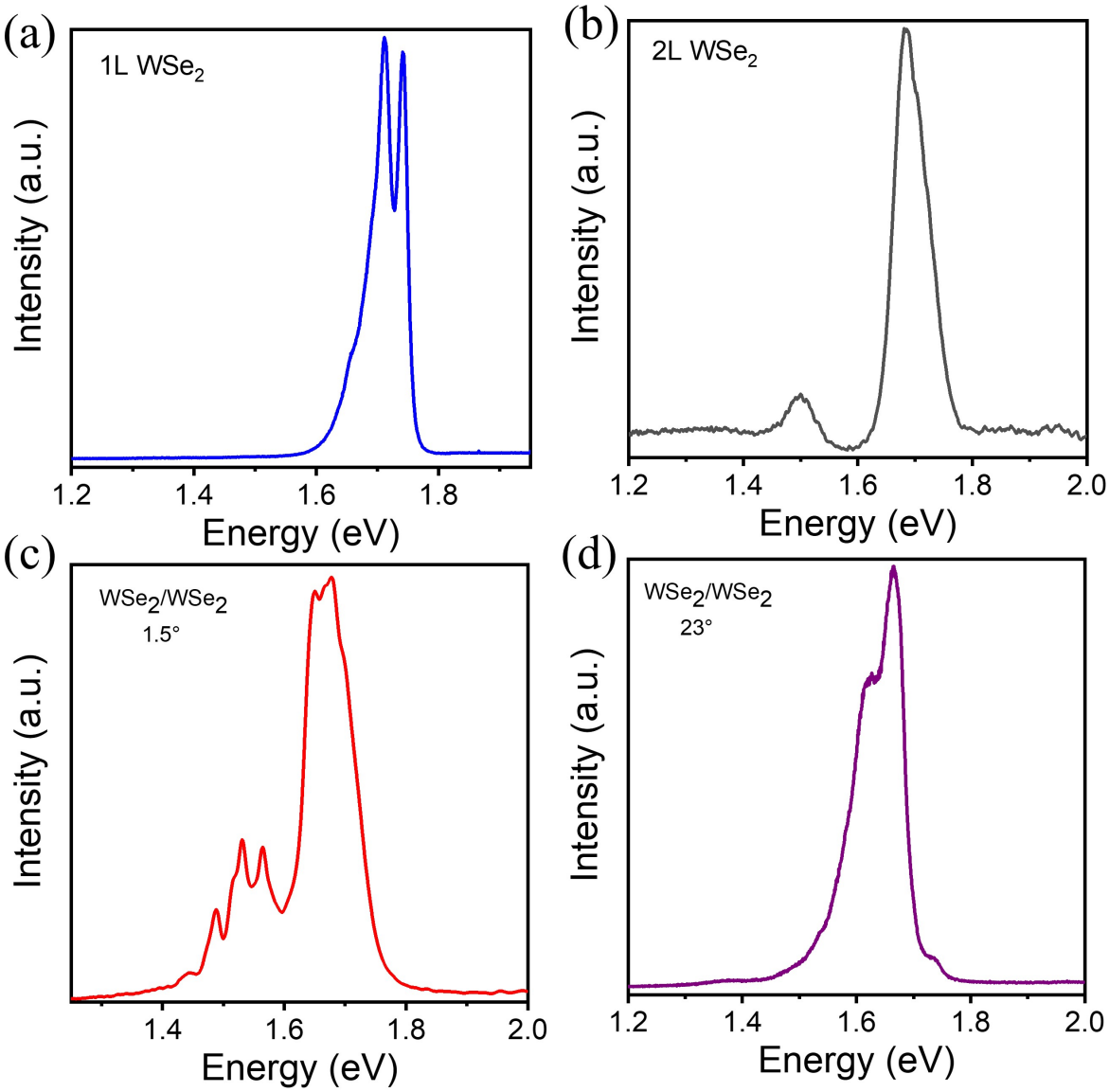

Supplementary Fig. 5 (a, b) Representative PL spectra of 1L-WSe_2 and 2L-WSe_2 at 10 K. (c, d) Representative PL spectra of 1L-WSe_2/WSe_2 homobilayer with a twist angle of 1.5° and 23° at 10 K under a low excitation power.

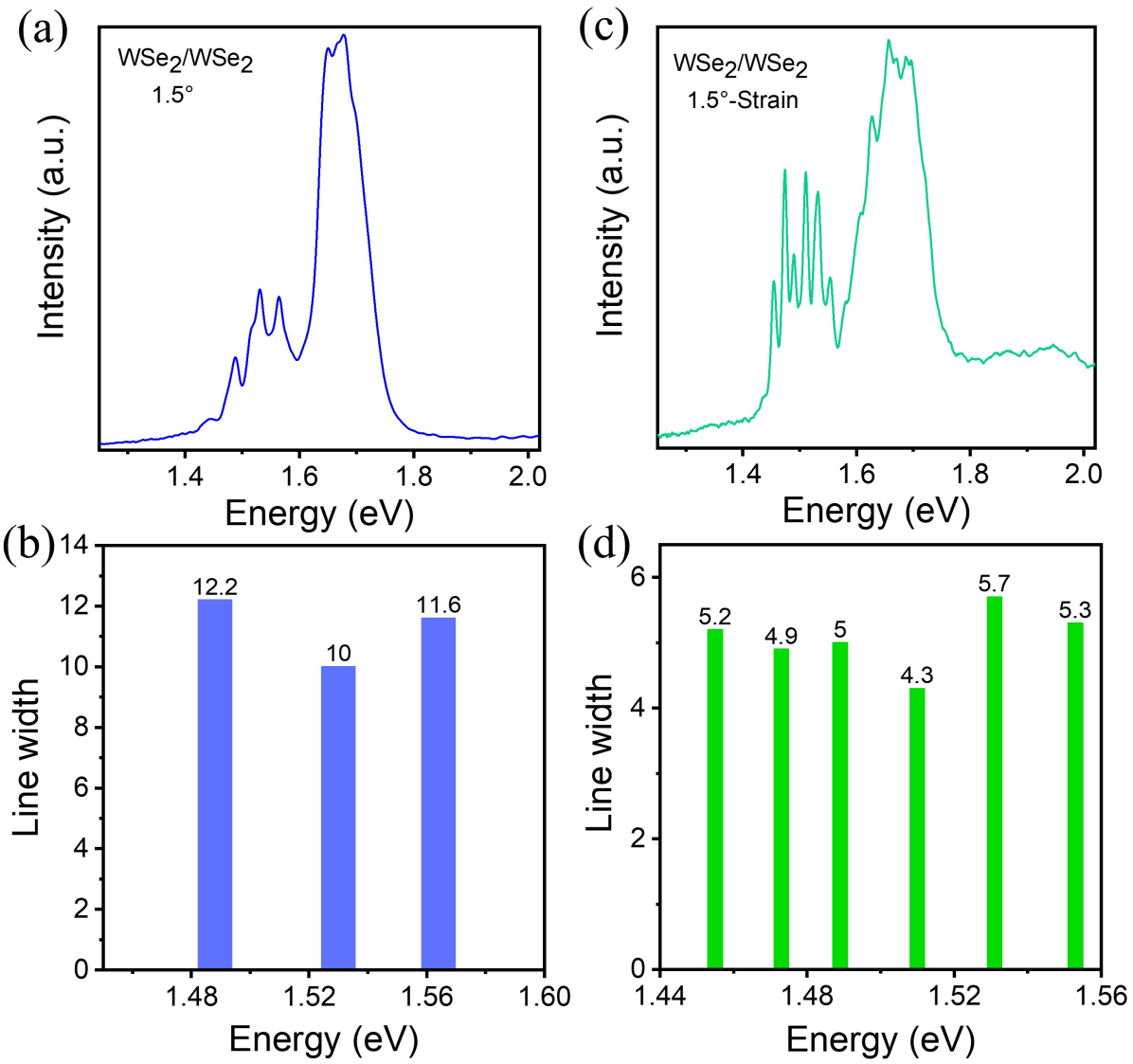

Supplementary Fig. 6 (a, b) Representative PL spectra of WSe_2/WSe_2 homobilayer with a twist angle of 1.5°. Line widths of moiré excitons of 12.2 meV, 10 meV and 11.6 meV are obtained for WSe2/WSe2 homobilayer. (c, d) Representative PL spectra of the twisted WSe_2/WSe_2 homobilayer on the Au NRAs. Line widths of moiré excitons of 5.2 meV, 4.9 meV, 5 meV, 4.3 meV, 5.7 meV and 5.3 meV are obtained for the twisted WSe_2/WSe_2 homobilayer on the Au NRAs.

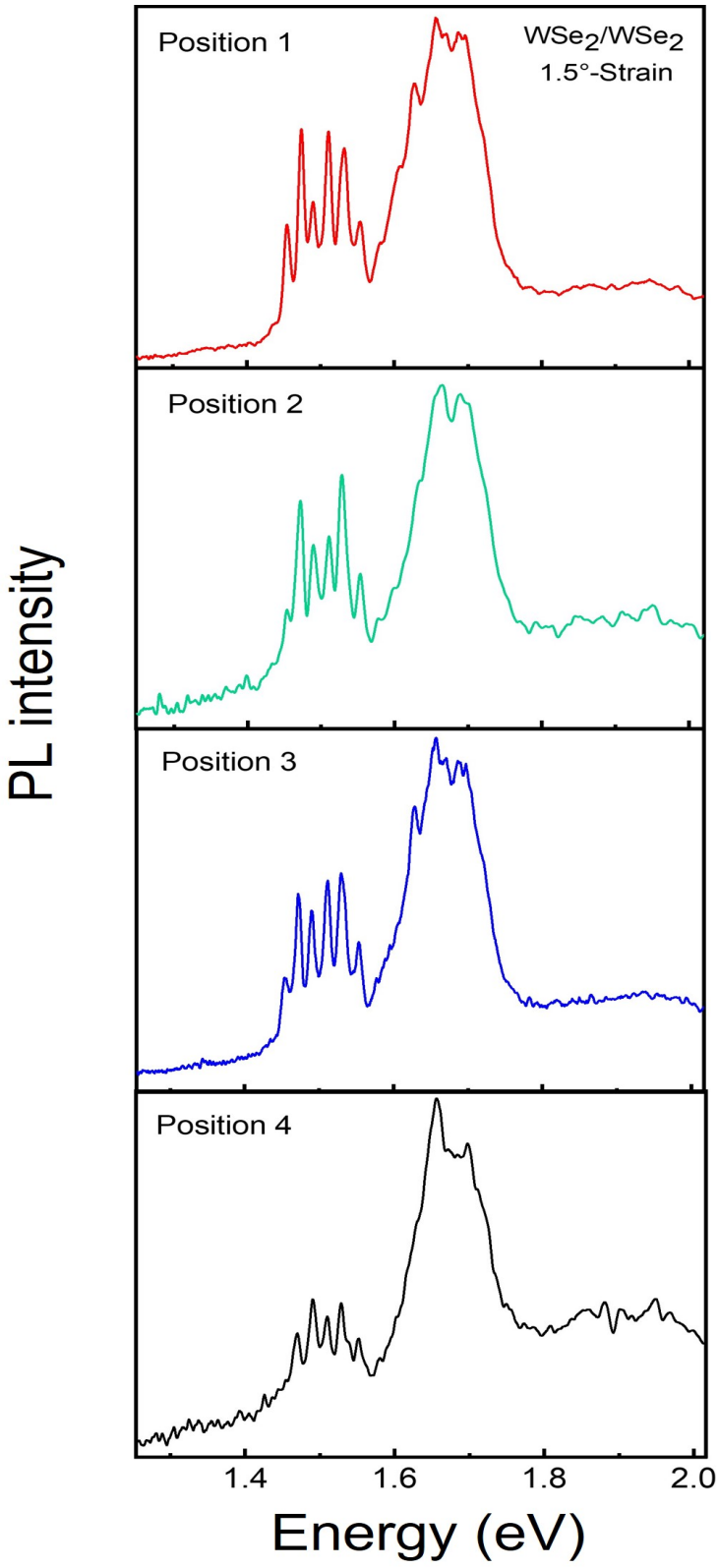

Supplementary Fig. 7 Photoluminescence (PL) spectra measured at four different positions in the sample of the twisted WSe_2/WSe_2 homobilayer on the Au NRAs at 10 K. The spatial homogeneity was observed in the twisted WSe_2/WSe_2 homobilayer on the Au NRAs.

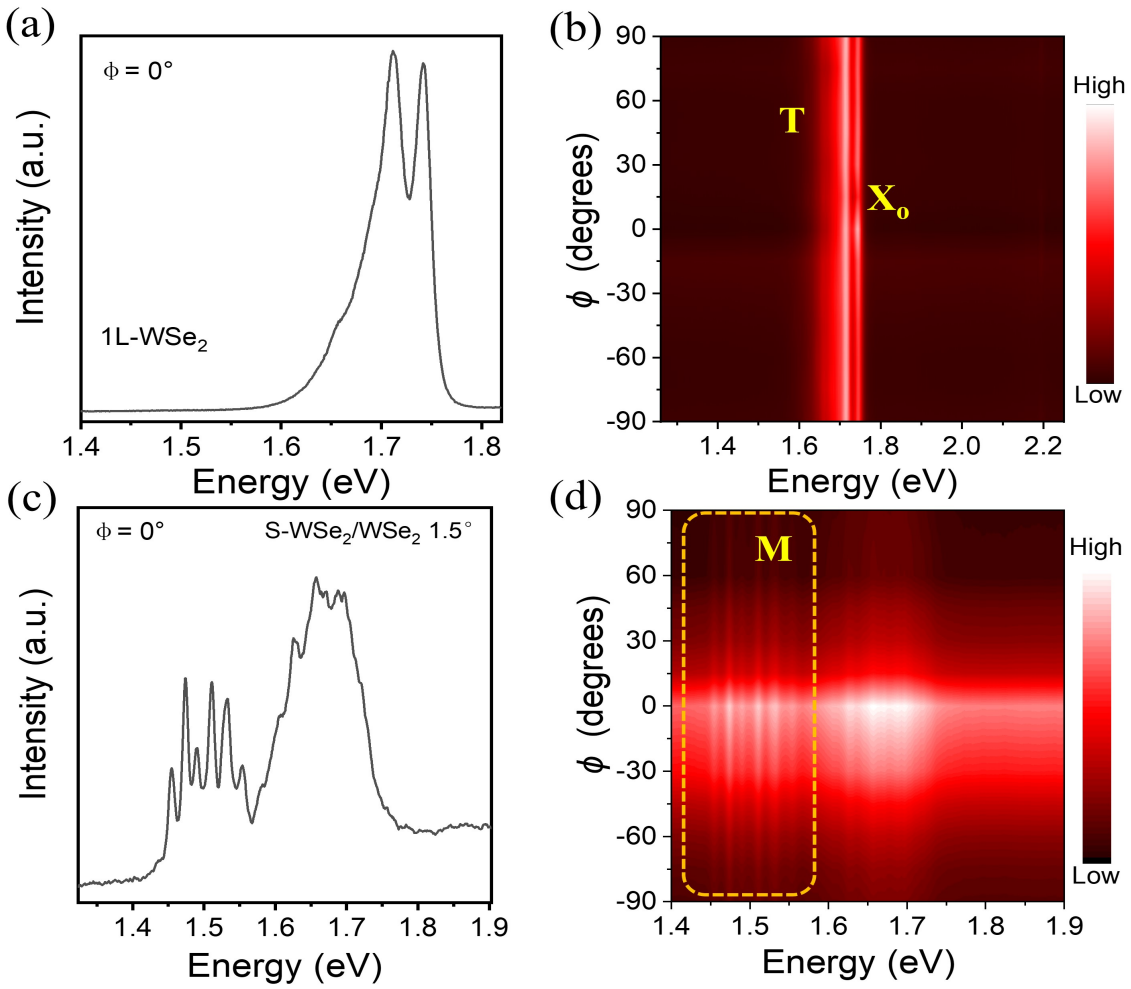

Supplementary Fig. 8 (a, b) Line tangent point of exciton energy in the monolayer WSe_2 as a function of the angle ϕ between the half-wave plate and linear polarizer. (c, d) Linear polarization spectra of the twisted WSe_2/WSe_2 homobilayers on the Au NRAs.

After comparing the linear polarization spectra of monolayer WSe_2 and twisted WSe_2/WSe_2 homobilayers on Au NRAs, we observed that the exciton of monolayer WSe_2 remained constant regardless of the linear polarization direction ϕ (Supplementary Fig. S8). This is because monolayer WSe_2 possesses C_3 symmetry, and its photoluminescence does not exhibit any linear polarization. Conversely, the excitons of twisted WSe_2/WSe_2 homobilayers on Au NRAs were influenced by linear polarization due to the strain in the homostructure. This resulted in an uneven distribution of positions of the emitted co-polarized and cross-polarized light.

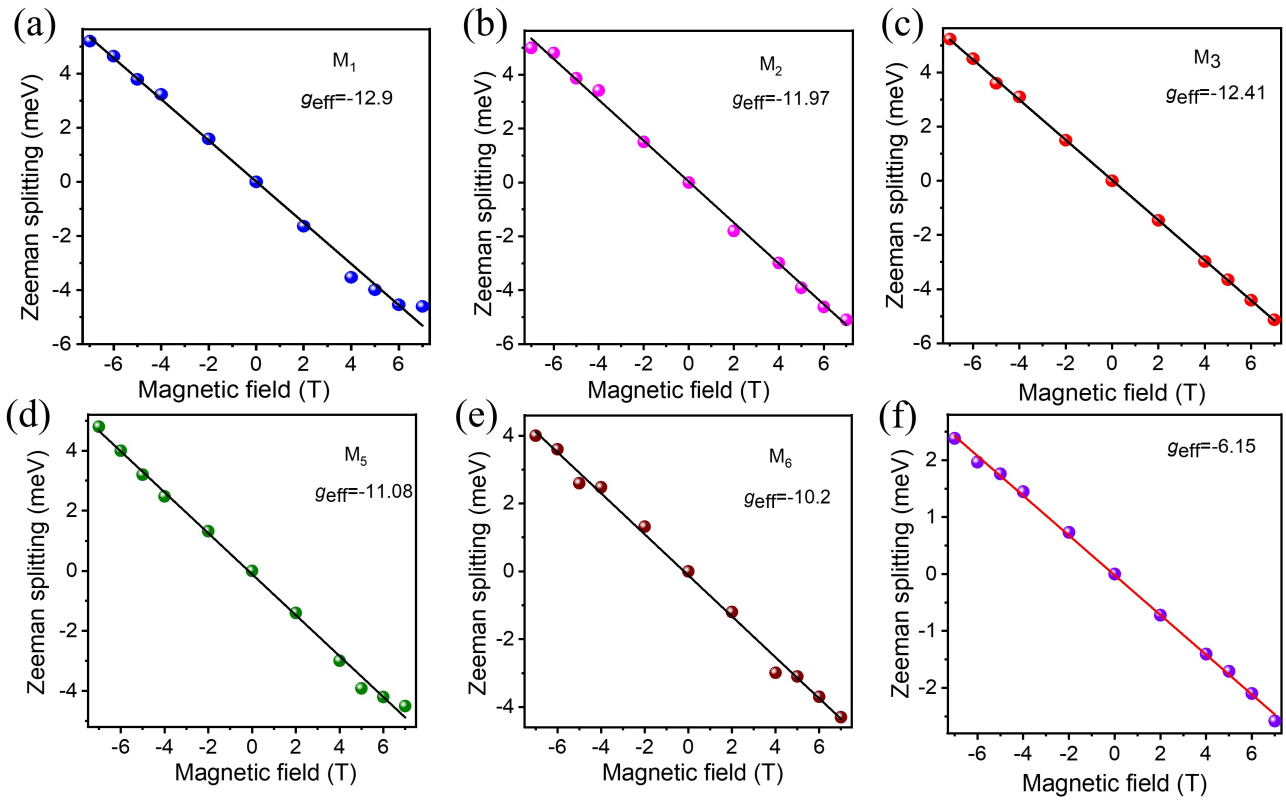

Supplementary Fig. 9 Zeeman splitting of the strain-localized moiré excitons in twisted WSe_2/WSe_2 homobilayer on the Au NRAs. (a-f) Zeeman splitting of the circularly polarized photoluminescence ($\Delta = E_{\sigma+} - E_{\sigma-}$) as a function of the magnetic field. The corresponding effective *g*-factors for the moiré excitons and neutral exciton are −12.9 ± 0.05, −11.97± 0.03, −12.41± 0.03, −11.08± 0.05, −10.2± 0.05 and -6.15 ± 0.05, respectively.

Supplementary Note 3. Simulation for the binding energy of interlayer biexciton in homostructure.

2D moiré superlattices provide a clean and precise platform for investigating moiré-trapped interlayer excitons. By stacking 2D materials with different lattice structures or twist angles, periodic moiré patterns can be generated, resulting in unique exciton miniribbons with a flat dispersion that significantly affect the correlation and dipole interactions of interlayer excitons. In atomically thin TMDCs, the interaction between interlayer excitons can be altered from dipole repulsion to attraction by adjusting the effective interlayer distance, which leads to the formation of a stable biexciton phase.

Additionally, the interlayer biexciton dipole in homostructures comprises two dipoles oriented in opposite directions, resulting in a negative inherent charge that increases its stability and attractive properties[1,2]. As a result, it is easier to form a stable biexciton phase in these systems (refer to Supplementary Fig. S10).

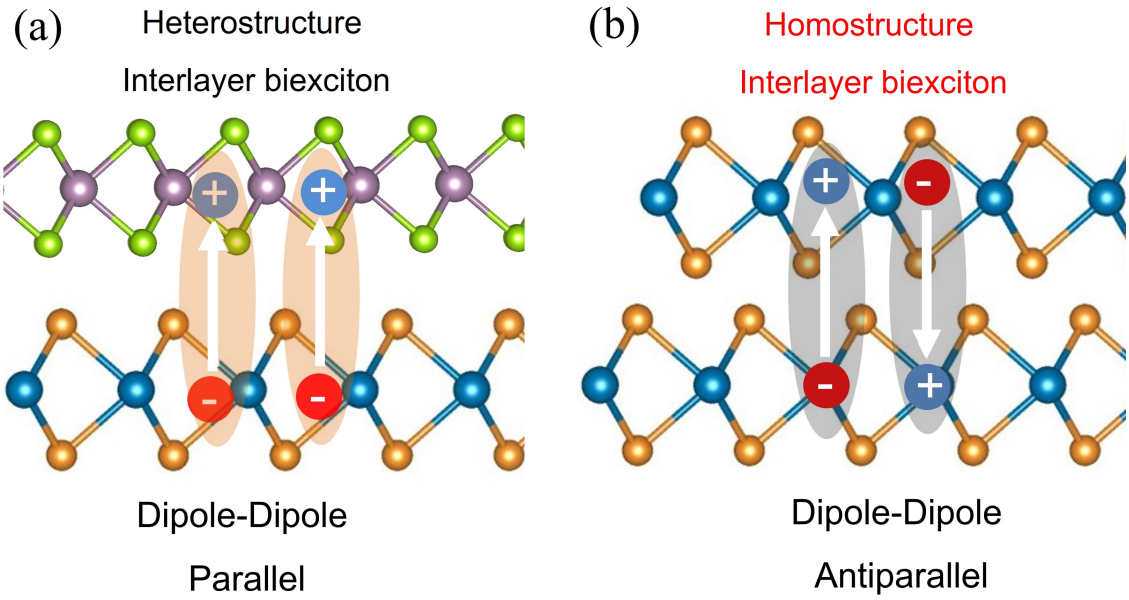

Supplementary Fig. 10 (a, b) Schematic diagram of heterostructure and homostructure of 2D materials, electrons and holes (red and blue circles, respectively) can be localized in the bottom, top layers, resulting in different kinds of strongly bound interlayer excitons. Vertical white arrows indicate the orientation of the permanent electric dipoles of different interlayer excitons.

For the first time, we have observed a unique transition from repulsion to attraction in a homostructure through dipolar interaction. The interaction energy between two interlayer excitons with parallel structure can be expressed as follows[3]:

$$E_{XX}(d) = -J_{XX}(\Delta\rho^{XX}) + \frac{2d^2}{(\Delta\rho^{XX})^3} - \frac{3d^2}{2(\Delta\rho^{XX})^5} \qquad (2)$$

The interaction energy between two interlayer excitons in an antiparallel structure can be represented as follows:

$$E_{XX}(d) = -J_{XX}(\Delta\rho^{XX}) - \frac{2d^2}{(\Delta\rho^{XX})^3} + \frac{3d^2}{2(\Delta\rho^{XX})^5} \quad (3)$$

The other parameters in the formula can be expressed as follows:

$$J_{XX}(\Delta\rho^{XX}) = \frac{2N^4}{3}\Delta\rho^{XX}\left(\frac{\alpha\Delta\rho^{XX}}{\sqrt{(\Delta\rho^{XX})^2+4d^2}} + \frac{1}{3(\alpha\Delta\rho^{XX}-1)}\right)\times \left(\frac{e}{3}\right)^{\frac{2\Delta\rho^{XX}}{\alpha\Delta\rho^{XX}-1}} \exp\left[-2\alpha\left(\sqrt{(\Delta\rho^{XX})^2+4d^2}-2d\right)\right] \quad (4)$$

$$\alpha = \frac{2}{1+2\sqrt{d}} \quad (5)$$

$$N = \frac{4}{\sqrt{1+4\sqrt{d}+8d(1+\sqrt{d})}} \quad (6)$$

The distance between layers is denoted by d. $\Delta\rho^{XX}$ is the lateral distance between the two interlayer excitons. The contribution of dipole and quadrupole interactions is represented by $\frac{2d^2}{(\Delta\rho^{XX})^3}$ and $\frac{3d^2}{2(\Delta\rho^{XX})^5}$.

The Bohr radii follows the equation below[4]:

$$a_B = \frac{4\pi\varepsilon_0\varepsilon_{eff}\hbar^2}{\mu e^2} \quad (7)$$

The vacuum permittivity and effective relative permittivity are expressed by ε_0 and ε_{eff}. μ is the reduced mass of an IX in the WSe_2/WSe_2 homostructure. $\hbar$ is the reduced Planck's constant. The interlayer distance d of the WSe_2/WSe_2 homostructure is 0.6 nm[5].

We define $\Delta\rho^{xx}$ as a variable with units of Bohr radius. The interaction energy, E_{xx}, can be numerically calculated as a function of $\Delta\rho^{xx}$ using formula (3). We calculated the interaction energy for both parallel and antiparallel structures (as shown in Table 1). When $\Delta\rho^{xx}$ is set to $1.55a_B$, the plot of E_{xx} for the antiparallel structure shows a *U*-shaped curve with a minimum energy of 0.4 R_y (Table 1). At this minimum energy point, the interlayer biexciton in the antiparallel structure is formed with a binding energy of approximately 55.39 ± 0.5 meV.

Table 1 : Simulation for the binding energy of interlayer biexciton in WSe_2/WSe_2 homostructure

	Dipole-Dipole Antiparallel	Dipole-Dipole Parallel
ε	4.64	4.477
a_B	11.157 Å	10.767 Å
R_y	138.97 meV	149.2 meV
E_B	55.39 meV	25.13 meV

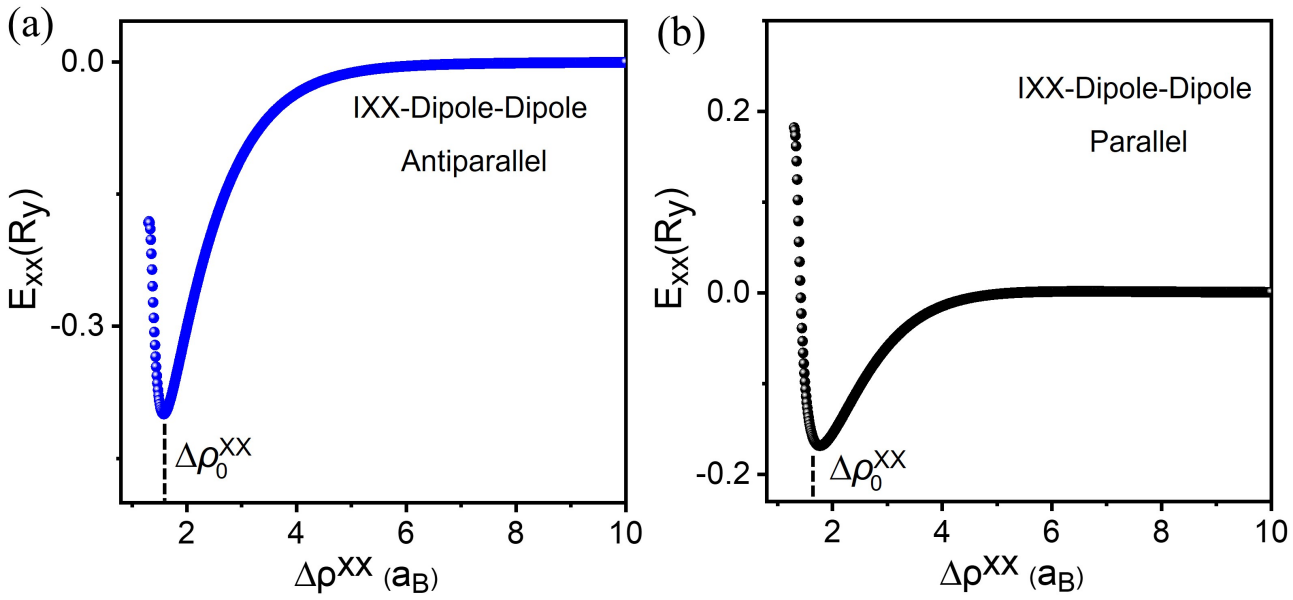

Supplementary Fig. 11 Calculation of interaction energy. The interlayer exciton interaction energy (a) with antiparallel configuration and (b) with parallel configuration (in unit of Rydberg energy R_y) is calculated as a function of the interlayer exciton distance $\Delta\rho^{XX}$ (in unit of Bohr radius a_B). E_{XX} shows a minimum energy at $\Delta\rho_0{}^{XX}$.

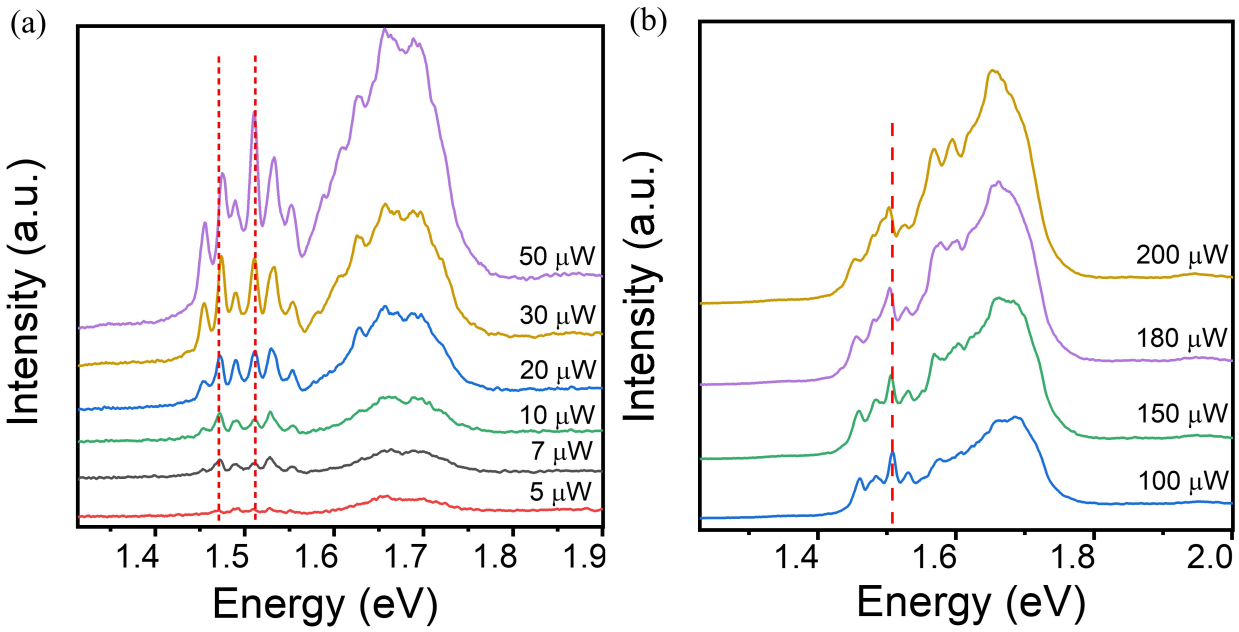

Supplementary Fig. 12 (a, b) PL spectra of the twisted WSe_2/WSe_2 homobilayers on the Au NRAs as a function of excitation power under 532 nm laser excitation at 10 K.

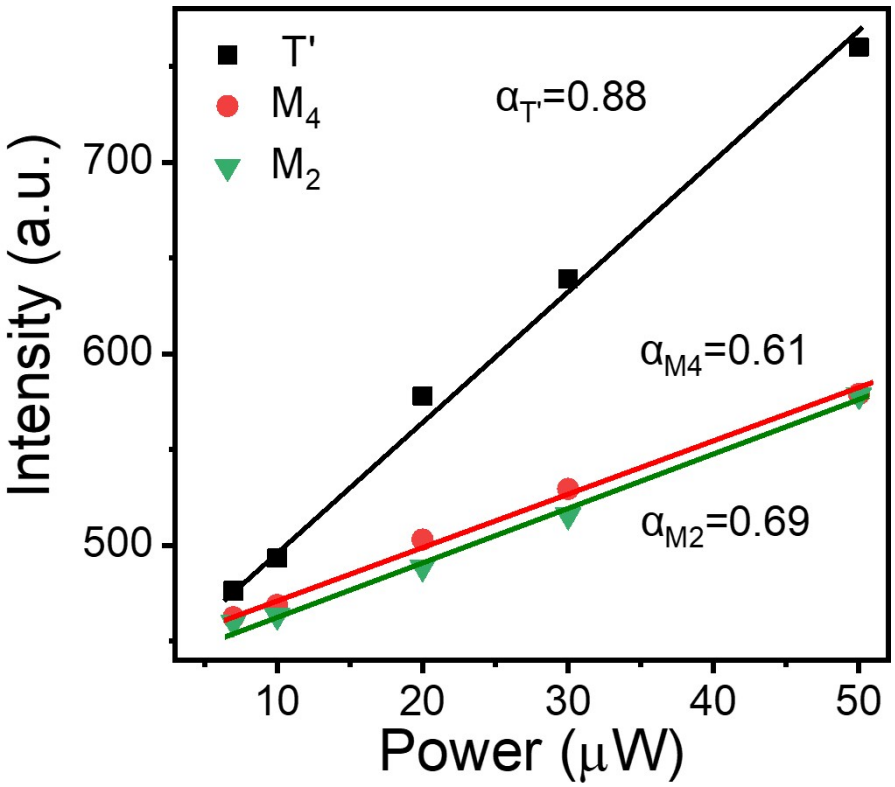

Supplementary Fig. 13 The PL intensity of T', M_2, M_4 peaks as a function of excitation power under 532 nm laser excitation at 10 K.

Supplementary Note 4. Estimation of the depth of moiré excitonic from the temperature-dependent PL intensity quenching.

To elaborate on the factors that affect moiré excitons, temperature, torsion angle, and the number of layers are the primary variables. To demonstrate our observation of moiré excitons in a twisted homobilayer, we analyzed the photoluminescence spectra as a function of temperature. The temperature-dependent PL intensity of excitons in the potential well can be obtained through the rate equation under the thermally-assisted process, as follows:

$$\frac{dN}{dt} = G - \gamma_{\mathrm{rad}}N - \gamma_{\mathrm{nrad}}N \qquad (8)$$

where G represents the formation rate of the trapped exciton. The variable N represents the population of excitons, which varies over time. The decay rates of the trapped excitons' radiative and nonradiative recombination processes are represented by γ_{rad} and γ_{nrad}, respectively. The nonradiative decay rate can be obtained from the rate equation as follows:

$$\gamma_{\mathrm{nrad}} = \gamma_0 \exp\left(-\frac{E}{k_{\mathrm{B}}T}\right) \qquad (9)$$

where γ_0 represent the rate constant. The thermal activation energy is denoted by E and corresponds to the potential depth. The PL intensity I can be expressed as:

$$I = I(0)\gamma_{\mathrm{rad}}N = I(0)\frac{G}{\left\{1+\frac{\gamma_0}{\gamma_{\mathrm{rad}}}\exp\left(-\frac{E}{k_{\mathrm{B}}T}\right)\right\}} \qquad (10)$$

The PL intensity at the lowest temperature limit can be expressed as *I(0)*. The $\frac{\gamma_0}{\gamma_{\mathrm{rad}}}$ refers to the pre-exponential parameter, which is determined by the ratio of the radiative recombination rate to the non-radiative recombination rate of the bound state.

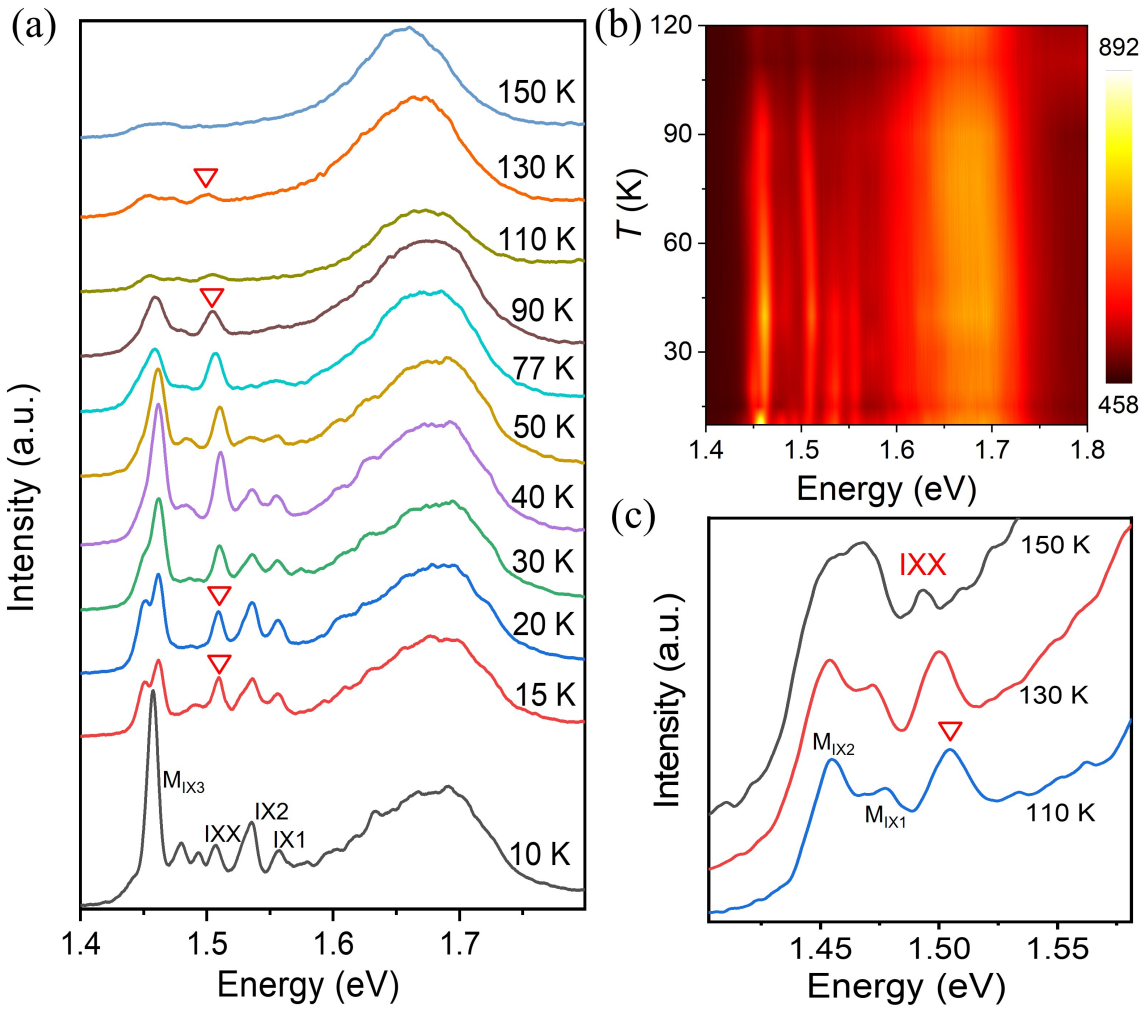

Supplementary Fig. 14 (a, c) The normalized PL spectra of the twisted WSe_2/WSe_2 homobilayers on the Au NRAs at various temperatures ranging from 10 to 150 K. (b) Contour plot of the temperature-dependent PL in the twisted WSe_2/WSe_2 homobilayers on the Au NRAs.

Figures S14a and S14b illustrate a contour map displaying the temperature-dependent PL spectra, revealing the origin of moiré excitons in twisted WSe_2/WSe_2 homobilayers on Au NRAs. Figure S14a displays the PL spectrum of the twisted WSe_2/WSe_2 homobilayers on Au NRAs at 10 K. The spectrum reveals multiple equally spaced splitting peaks at 1.45 to 1.6 eV, primarily caused by exciton capture by the moiré potential in the twisted WSe_2/WSe_2 homobilayers. The IX1, IX2, IXX, M_{IX1}, M_{IX2}, and M_{IX3} peaks represent the interlayer excitons trapped by the moiré potentials, while T' represents the trion exciton peaks.

As the temperature rises, the moiré exciton peaks gradually vanish, and all PL peaks shift to the red due to the temperature-dependent bandgap shift. Figure S14a displays the PL spectra from 10 to 150 K obtained from the horizontal line cut of the contour map. As the temperature increases, the PL intensity of the low-energy state decreases rapidly and disappears at temperatures above approximately 150K (Supplementary Fig.14c). The luminescence intensity of the low-energy emission is strongly suppressed as temperature increases, mainly due to the thermal dissociation and thermal excitation of the exciton-bound state. With increasing temperature, the moiré excitons gain more energy and are more likely to dissociate from the moiré potential. The critical temperature for the disappearance of moiré excitons further demonstrates that the strain-induced localized moiré excitons offer a promising avenue for observing moiré excitons at room temperature.

Supplementary Note 5. First-principles calculation of the bandgaps of the WSe_2/WSe_2 bilayer homostructure.

(1) Computational method

We utilized the Vienna ab initio simulation package (VASP) [6], employing the projected augmented wave potential to perform density functional theory (DFT) calculations[7]. The exchange and correlation functional were treated with the generalized gradient approximation developed by Perdew–Burke–Ernzerhof (GGA-PBE) [8]. The interlayer van der Waals (vdW) interaction was simulated using the DFT-D_3 method with Becke-Jonson damping[9,10]. The plane wave basis set utilized valence states $5d^5 6s^1$ for W and $4s^2 4p^4$ for Se, with an energy cutoff of 400 eV. To fully optimize the atomic geometry in each moiré superlattice, we relaxed all atoms until the residual force on each atom was less than 0.01 eV/Å, and we set the energy convergence criterion at 10^{-4} eV. We also calculated electronic band structures along the high symmetry M-Γ-K-M paths in the Brillouin zone (BZ) for each superlattice, with a

vacuum layer of approximately 20 Å in the Z direction.

(2) Comparison of the electronic structures of 1L, 2L WSe_2 lattice without twist angle

The 1L WSe_2 structure is characterized by a 3-atom hexagonal unit cell with P-6m2 ($D3h^1$, No. 187) symmetry, where the equilibrium lattice parameters are a = 3.2511 Å and c = 24 Å. One W atom and two Se atoms occupy 1*d* (1/3, 2/3, 0.5) and 2*i* (2/3, 1/3, 0.4304) Wyckoff positions, respectively. In Fig. S15(a), we can observe the electronic band structure of 1L WSe_2, which demonstrates that it is a semiconductor with an indirect band gap of 1.686 eV. The CBM is located at *q* between the Γ and K points with a lowest conduction bandwidth of 1442 meV, while the VBM is located at the K point with a highest valence bandwidth of 1232 meV. It is noteworthy that the direct band gap of 1.745 eV at the K point is relatively close to the indirect band gap, indicating that 1L WSe_2 is a semiconductor with a quasi-direct band gap.

The bulk-like AB stacking of 2L WSe_2 has a hexagonal unit cell consisting of 6 atoms in P-3m1 ($D3d^3$, No. 164) symmetry. The equilibrium lattice parameters are a = 3.2513 Å and c = 32 Å. In this structure, 2 W atoms and 4 Se atoms occupy the 2*d* (1/3, 2/3, 0.40)-W, 2*d* (1/3, 2/3, 0.6522)-Se_1, and 2d (1/3, 2/3, 0.5477)-Se_2 Wyckoff positions, respectively. The electronic band structure is shown in Fig. S15(b), indicating that 2L WSe_2 is a semiconductor with an indirect band gap of 1.306 eV. The CBM is located between the Γ and K points, with a lowest conduction bandwidth of 1640 meV. The VBM is located at the Γ point, with the highest valence bandwidth being 1303 meV. Additionally, the direct band gap at the K point is estimated to be 1.689 eV, which is much larger than the indirect band gap, indicating that 2L WSe_2 is an indirect semiconductor.

Based on the results above, we can observe that as the number of layers increases, the VBM (valence band maximum) shifts from the K point (in 1L WSe_2) to the Γ point (in 2L WSe_2), and the

minimum q point of the conduction band gradually decreases. Consequently, the bandgap of the WSe_2 material also decreases gradually.

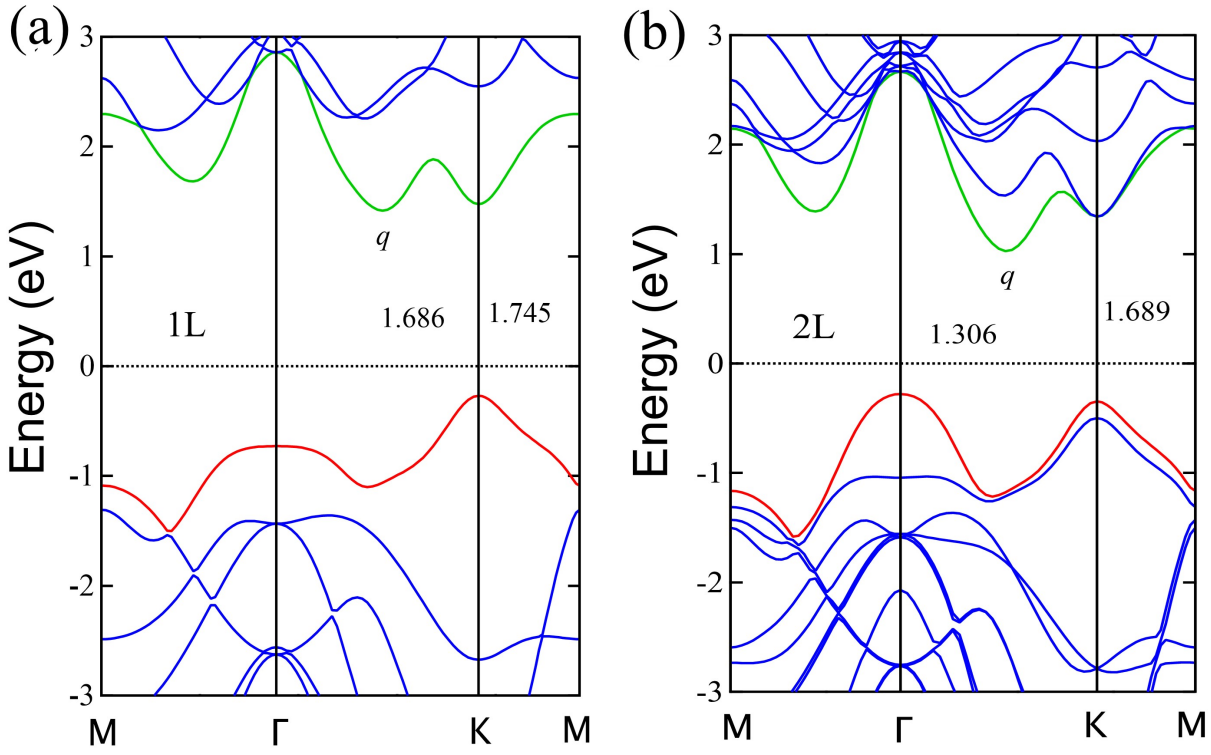

Supplementary Fig. 15 (a, b) Electronic structures of 1L, 2L WSe_2 without twist angle ($\theta = 0$).

(3) Electronic band structures for 1L/1L WSe_2 moiré superlattice

Figure S16(a) shows the moiré superlattice (MSL) of 1L/1L WSe_2 with a twist angle of approximately 3.2° [11]. The MSL consists of 662-W and 1324-Se atoms arranged in a hexagonal unit cell with P321 (D32, No. 150) trigonal symmetry. The equilibrium lattice parameters are $a_M = b_M =$ 59.1376 Å ($a_M/b_M = 1$). To investigate the effect of strain, we adjusted the lattice parameters to $a_M =$ 60.9117 Å and $b_M =$ 59.1376 Å ($a_M/b_M = 1.03$) and optimized the atom positions accordingly.

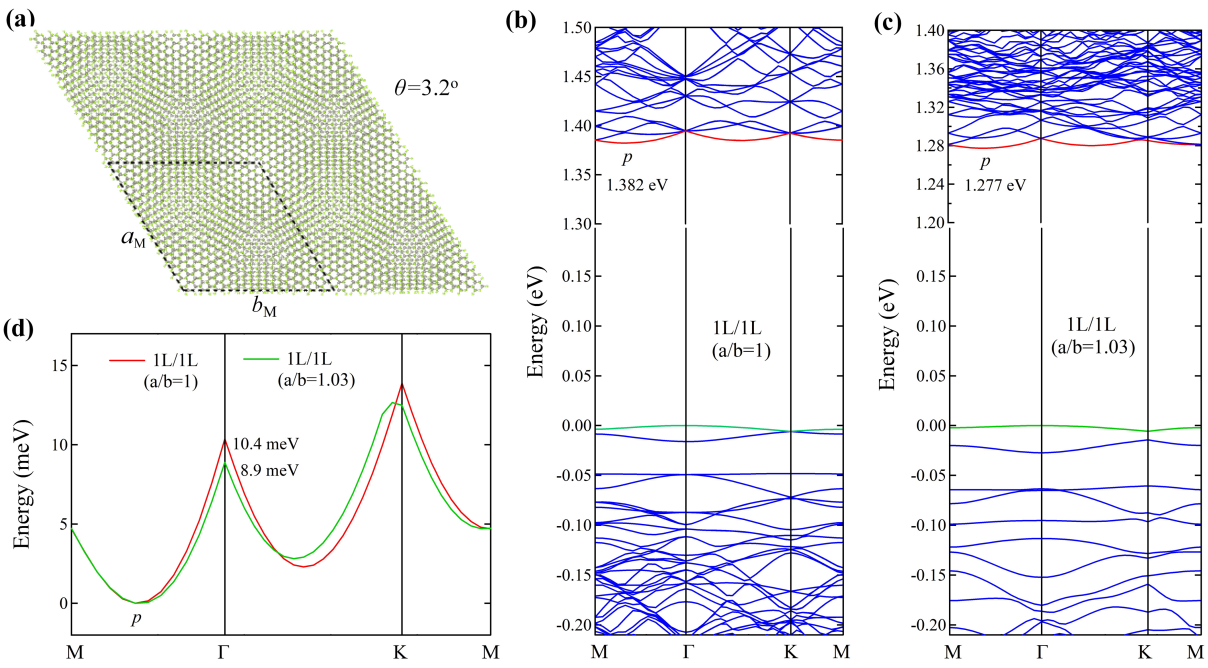

Supplementary Fig. 16 (a) Top view for 1L/1L WSe_2 moiré superlattice in *P321* (D_3^2, No. 150) trigonal symmetry with a twist angle of 3.2 °. (b, c) Band structures of 1L-WSe_2/1L-WSe_2 (a_M/b_M=1) and 1L-WSe_2/1L-WSe_2 (a_M/b_M=1.03) moiré superlattices. The Fermi level is set to zero eV, the valence band maximum at the Γ point, while the conduction band minimum at the *p* point. (d) The moiré potentials measured as the difference between the lowest conduction band and highest valence band. It is estimated to be 10.4 and 8.9 meV for 1L-WSe_2/1L-WSe_2 (a_M/b_M=1) and 1L-WSe_2/1L-WSe_2 (a_M/b_M=1.03) moiré superlattices, respectively.

Figure S16 (b) and (c) depict the electronic band structures of moiré superlattices of 1L-WSe_2/1L-WSe_2 (a_M/b_M=1) and 1L-WSe_2/1L-WSe_2 (a_M/b_M=1.03), respectively. Our study reveals that the 1L/1L MSL (a_M/b_M=1.03) behaves as a semiconductor with an indirect band gap of 1.277 eV [see Figure S16 (c)], which is smaller than the band gap of 1.382 eV observed for 1L/1L MSL (a_M/b_M=1) [see Figure S16 (b)]. The valence band maximum (VBM) is situated at the Γ point, while the conduction band minimum (CBM) is located at p between the M (0, 1/2, 0) and Γ(0, 0, 0) points. The valence band is flat, with a maximum valence bandwidth of only 6 meV and the lowest conduction bandwidth of 10 meV, similar to the findings observed in Figure S16 (b) for 1L-WSe_2/1L-WSe_2 (a_M/b_M=1).

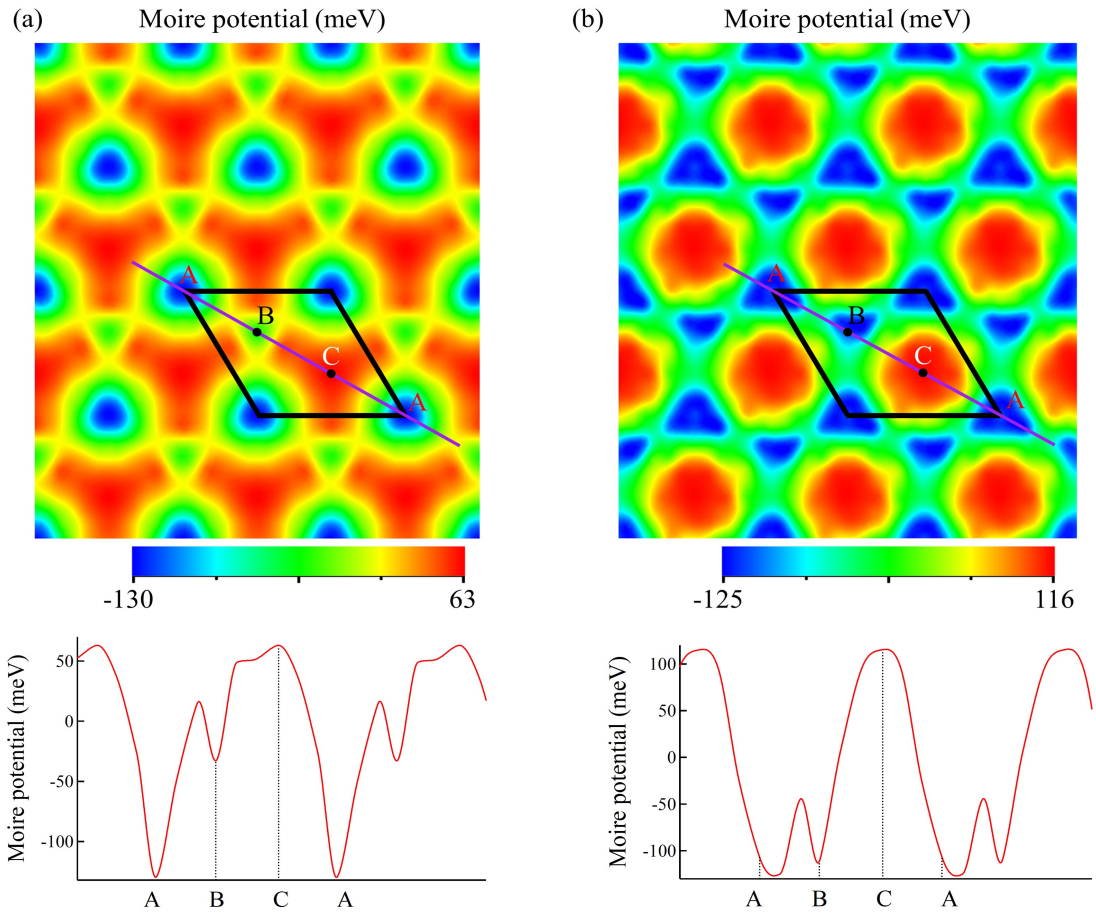

Supplementary Fig. 17 (a, b) The bandgap changes of 2L(A/B) WSe_2 are obtained when the A-layer atoms are fixed and the B-layer atoms are moved by one primitive unit cell along the *x* and *y* directions. In (a) For 1L/1L WSe_2 without strain (a=b=3.2753 Å), the maximum moiré potential depth of the WSe_2 bilayer superlattice is 193 meV; In (b) for 1L/1L WSe_2 with a 3% tensile strain (a=3.3754 Å, b=3.2753 Å), the maximum moiré potential depth of the WSe_2 bilayer superlattice is 241 meV.

References

1. Stern, M., Umansky, V. & Bar-Joseph, I. Exciton liquid in coupled quantum wells. *Science* **343**, 55–57 (2014).
2. Nagler, P. et al. Interlayer exciton dynamics in a dichalcogenide monolayer heterostructure. *2D Mater.* **4**, 025112 (2017).
3. Bondarev, I. V. & Vladimirova, M. R. Complexes of dipolar excitons in layered quasi-two-dimensional nanostructures. *Phys. Rev. B* **97**, 165419 (2018).
4. Lee, R., Drummond, N. & Needs, R. Exciton-exciton interaction and biexciton formation in bilayer systems. *Phys. Rev. B* **79**, 125308 (2009).
5. L.A. Jauregui et al, Electrical control of interlayer exciton dynamics im atomically thin heterostructures, *Science* **366**, 870 (2019).
6. Kresse, G.; Furthmüller, J., Efficient iterative schemes for ab initio total-energy calculations sing a plane-wave basis set. *Physical review. B*, Condensed matter 1996, **54** (16), 11169-11186.
7. Blöchl, P. E., Projector augmented-wave method. *Physical Review B* 1994, **50** (24), 17953-17979.
8. Perdew, J. P.; Burke, K.; Ernzerhof, M., Generalized Gradient Approximation Made Simple. *Physical Review Letters* 1996, **77** (18), 3865-3868.
9. Grimme, S.; Antony, J.; Ehrlich, S.; Krieg, H., A consistent and accurate ab initio parametrization of density functional dispersion correction (DFT-D) for the 94 elements H-Pu. *The Journal of Chemical Physics* 2010, **132** (15), 154104.
10. Grimme, S.; Ehrlich, S.; Goerigk, L., Effect of the damping function in dispersion corrected density functional theory. *Journal of Computational Chemistry* 2011, **32** (7), 1456-1465.
11. Wu, B.; Zheng, H.; Li, S.; Chang-Tian Wang, C. T.; Ding, J.; He, J.; Liu, Z.; Wang, J. T.; Liu, Y., Effect of layered-coupling in twisted WSe_2 moiré superlattices, *Nano Res*. (2022).